

Treatment of Forced Flap Motions for Aeroelastic Simulations of an Arrow Wing

Abdul M. Rampurawala* and Ken J. Badcock†

CFD Laboratory, Dept. of Aerospace Engineering, University of Glasgow, G12 8QQ, United Kingdom

This study describes a CFD based simulation of an oscillating trailing edge control surface on a flexible arrow wing. The computed unsteady surface pressure distribution and the deformation of the wing due to the control surface oscillation are validated against experimental results. The structure of the wing is modelled so that the first wing bending mode resonates with the flap oscillating frequency (FOF) of 15 Hz as observed in the experiments. A predefined flap mode is applied to the surface grid to implement the forced flap oscillations. The FEM package NASTRAN is used to model the structure and the CFD code PMB developed at University of Glasgow is used for the simulations.

I. Introduction

One of the identified areas for future Computational Aeroelasticity (CAE) research is computational aeroservoelasticity.¹ One of the first computational forced flap oscillation studies was performed by Bharadvaj on the F5 and HARW wing configurations.² Forced flap oscillations using the unsteady RANS equations were performed over the F-5 wing and a clipped delta wing by Obayashi and Guruswamy using the CFD code ENSAERO³ while Obayashi *et al.* analysed a full span rigid arrow wing with symmetric and anti-symmetric oscillating control surfaces.⁴ Klopfer and Obayashi developed and implemented a virtual zone technique for the treatment of oscillating control surfaces. This was applied to a clipped delta wing and the computed results were validated against experiments.⁵ Unsteady pressure distribution due to an oscillating trailing edge control surface was calculated over a 55° delta wing using the Euler equation based code EURANUS by Karlsson.⁶ A transpiration boundary condition was applied to treat the oscillating flap by Cole *et al.* to simulate a Benchmark Active Control Technology (BACT) case⁷ and the unsteady pressure distribution compared with the experiments. Flutter suppression and alleviation by Active Control Technology (ACT)^{8,9} and prediction of control surface reversal due to wing flexibility¹⁰ has been the motivation for many of computational aeroservoelasticity simulations. The BACT wing has a rich database for the validation of aeroelastic and aeroservoelastic computations. Computations for unsteady pressure prediction have been performed on the BACT case by Schuster in the subsonic regime though this did not include prediction of dynamic deformation.¹¹

As most aircraft wings are flexible up to some extent, a more representative case is of an oscillating control surface on a flexible structure. The unsteady pressure distribution over the wing due to control surface oscillations results in dynamic structural deflections. Moreover the FOF frequency may resonate with the natural frequency of vibration of the structure causing large deformations. Such a simulation is the topic of the current study.

The Japan Aerospace Exploration Agency (JAXA)^a, as part of the Japanese SST program, is developing an experimental Supersonic Transport model and a wind tunnel model of this was tested in the transonic regime for unsteady pressure and dynamic deformation.^{12,13} The purpose of the experiment was to accumulate verification data for the validation of aeroelastic codes and active control technology. The experimental data from this work was used in the current study.

Control surfaces are important components of an aircraft. Apart from performing the necessary manoeuvring functions, they are also required for the operational efficiency and agility of the aircraft. For these

*PhD Student, CFD Laboratory, Student Member.

†Reader, Dept. of Aerospace Engineering., Member

^aformerly National Aerospace Laboratory

reasons it is important that they are free of any structural or aerodynamic instabilities. The deployment of control surfaces can be accompanied by deformation of the wing structure due to pressure redistribution over the wing. In special cases, for some wings, if the local deformation is large enough it can result in a control surface reversal. Prediction of structural deformation due to control surface deflection for such cases is important to prevent the aircraft encountering such phenomenon. Another instability encountered is at transonic Mach numbers when the shock oscillates over the trailing edge control surface. This can lead to shock induced instabilities of the control surface and is an issue for supersonic transport aircraft with thin trailing edge flaps. The lack of space at the trailing edge in these configurations prevent adequate constraints to be applied to the control surface. The study of shock oscillation over the control surface is important in these cases. The purpose of the current paper is to computationally predict the dynamic deformation and pressure distribution that are brought about by the forced oscillation of the control surface in transonic flows. Development of this ability is a step towards treating control surface instabilities on aircraft.

II. CAE Methodology

All computations were performed using the Parallel Multi-Block (PMB) flow solver¹⁴ developed at the University of Glasgow, which has been continually revised and updated over a number of years. The solver has been successfully applied to a variety of problems including cavity flows, hypersonic film cooling, spiked bodies, flutter and delta wing flows amongst others. The fluid and structural equations are solved on separate grids. The aerodynamic force is calculated over the fluid surface grid and is interpolated to the structural grid using the Constant Volume Tetrahedron (CVT) transformation scheme.¹⁵ The deformation on the structural grid is calculated using the modal FEM solver and the fluid surface grid is updated using the latest deformation. To minimise the sequencing errors the fluid and structural equations are coupled in pseudo time.¹⁶ For the forced flap oscillations the flap deflection angle is incremented in real time and the structural response due to pressure redistribution is updated in pseudo time with the flow.

A. CFD solver

The code solves the unsteady Reynolds Averaged Navier-Stokes equations, in serial or parallel mode on multi-block structured grids. The equations are discretised using a cell-centred finite volume method. The convective terms are discretised using either Osher's or Roe's scheme. MUSCL interpolation is used to provide nominally third order accuracy and the Van Albada limiter is used to avoid spurious oscillations across shocks. The time-marching of the solution is based on an implicit, dual time-stepping method. The final algebraic system of equations is solved using a Conjugate Gradient method, in conjunction with Block Incomplete Lower-Upper factorisation. A number of turbulence models including one and two-equation statistical models as well as Large-Eddy Simulation (LES) and Detached Simulation (DES) formulations have been implemented into the code. More details on the PMB solver can be found in Badcock et. al.¹⁴ In the current work the $k - \omega$ turbulence model was used for all the viscous calculations.

B. Structural solver

Finite element methods allow for the static and dynamic response of a structure to be determined. Stiffness (\mathbf{K}) and mass (\mathbf{M}) matrices are used to determine the equation of motion of an elastic structure subjected to an external force \mathbf{f}_s as

$$\mathbf{M}\delta\ddot{\mathbf{x}}_s + \mathbf{K}\delta\mathbf{x}_s = \mathbf{f}_s \quad (1)$$

where $\delta\mathbf{x}_s$ is a vector of displacements on a grid of points \mathbf{x}_s . Because the structural system under consideration is assumed to be linear, its characteristics are determined once and for all prior to making the flutter calculations, so that \mathbf{M} and \mathbf{K} are constant matrices generated, in this case, by the commercial package NASTRAN.

The aircraft deflections $\delta\mathbf{x}_s$ are defined at a set of grid points \mathbf{x}_s by

$$\delta\mathbf{x}_s = \sum \eta_i \phi_i \quad (2)$$

where ϕ_i are the mode shapes and η_i the generalised displacements. Here the η_i depend on time but the mode shapes do not. The values of ϕ_i and ω_i are calculated by solving the eigenvalue problem

$$[\mathbf{M} - \omega_i^2 \mathbf{K}]\phi_i = \mathbf{0}. \quad (3)$$

The eigenvectors are scaled so that

$$[\phi_i]^T \mathbf{M}[\phi_i] = 1. \quad (4)$$

Projecting the finite element equations onto the mode shapes results in the equations

$$\frac{d^2 \eta_i}{dt^2} + \omega_i^2 \eta_i = \phi_i^T \mathbf{f}_s \quad (5)$$

where \mathbf{f}_s is the vector of external forces at the structural grid points. This equation can be solved by a two stage Runge-Kutta method, which requires a knowledge of \mathbf{f}_s^n and \mathbf{f}_s^{n+1} . To avoid introducing sequencing errors by approximating the term \mathbf{f}_s^{n+1} the Runge-Kutta solution is iterated in pseudo time along with the fluid solution i.e. the latest estimate for \mathbf{f}_s^{n+1} is used in the Runge Kutta solution. At convergence of the pseudo time iterations the structural and fluid solutions are properly sequenced in time. It should be noted that the cost of the coupled calculation resides with the CFD solver when modal structural models are used. The CFD solver used in the current work is of good efficiency in the sense that the time step is always chosen to adequately resolve the solution temporally and is never chosen to facilitate the operation of the solver due to stability or any other numerical considerations.

C. Mesh movement

The geometries of interest deform during the motion and the mesh must be moved to conform with the evolving geometry. This is achieved using Transfinite Interpolation (TFI) of displacements within the blocks containing the aircraft. The surface deflections are interpolated to the volume grid points \mathbf{x}_{ijk} as

$$\delta \mathbf{x}_{ijk} = \psi_j^0 \delta \mathbf{x}_{a,ik} \quad (6)$$

where ψ_j^0 are values of a blending function¹⁷ which varies between one at the aircraft surface and zero at the block face opposite. The surface deflections $\mathbf{x}_{a,ik}$ are obtained from the transformation of the deflections on the structural grid and so ultimately depend on the values of the generalised structural coordinate η_i . The grid speeds can be obtained by differentiating equation (6) to obtain their explicit dependence on the values of η_i .

III. The Experimental Model

The current study is based on the transonic aeroelastic experiments performed at NAL-Japan.¹² One of the motivations for the experiments was to generate a set of results against which aeroelastic codes could be validated. For this reason, along with the unsteady pressure distribution over the wing, parameters like dynamic deformation and unsteady force coefficients were also measured.

The SST arrow wing is a cranked double delta with a root chord of 2.103 metres. A half model is used in the experiments with a semi-span of 1 metre. The section profile is a NACA 0003. The inboard delta has sweep angle of 72.8° and the outboard a sweep of 51.6° . The trailing edge flap starts at 20% half-span and terminates at 50% half-span. The flap chord is 0.11 metres. Figure 1 shows the dimensions of the experimental model in millimeters. Experimental data is available for a range of Mach numbers between 0.79 and 0.91, angles of attack of 0° , -2° and -4° , flap mean angles of 0° , -5° and 5° and FOFs of 5 Hz, 10 Hz, 15 Hz, 20 Hz, 25 Hz and 30 Hz.

Along with the measured unsteady pressure and deformation, FEM data in the form of a structural grid and computed natural modes of vibration are also provided in the paper.¹² A brief description of the structure of the experimental model is presented in an earlier paper by Tamayama.¹³ As described in the

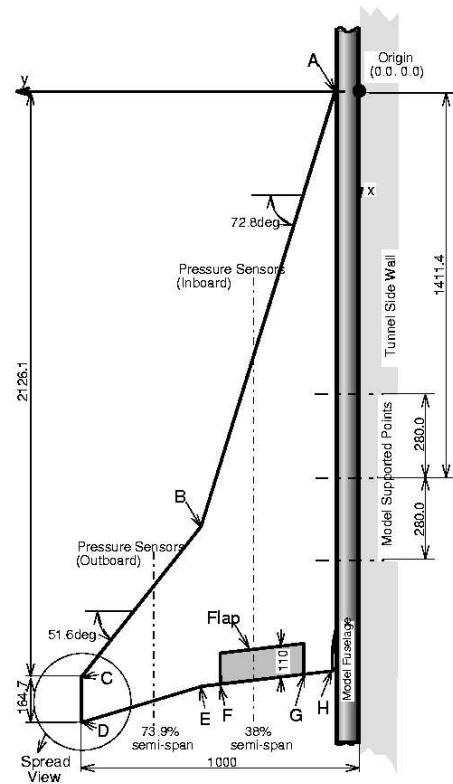


Figure 1. The SST Arrow Wing.

paper the wing structure is made up of a 7 mm thick aluminium plate with holes drilled to make it flexible. It was found in the experiments that the frequency of the first wing bending mode increased from 9.79 Hz at no-flow conditions to around 15 Hz at Mach 0.8.¹³ As the frequency of this mode lies in the vicinity of the forced FOFs (5 Hz-30 Hz) and as the frequency of the next natural mode is a lot higher (40.25 Hz) almost all the deformation of the structure is contributed by the first wing bending mode. It was observed in the experiments that this mode stiffened in the flow and coupled with the FOF of 15 Hz. This means that the maximum wing dynamic deformations occur at a FOF of 15 Hz. To get a good comparison of computed dynamic deformation with the experiments it is required that the first wing bending mode couples with the right oscillating frequency.

It was found in the current study that the FEM model provided in the paper presenting the experimental results¹² did not resonate with the FOF of 15 Hz. This might be due to the fact that in the given flow conditions the FEM model does not stiffen as much in the computations as observed in the experiment. To test this an aeroelastic simulation was performed with the given FEM model and the flow conditions described in the experiment.¹³ A small impulse was given to the wing and the frequency of the oscillation was measured. At Mach 0.8 and a dynamic pressure of 23.35 kPa the frequency of the first wing bending mode increased from 11.09 Hz to 12 Hz instead of to 15 Hz as quoted in the experiments. Due to this the resonance between the flap oscillations and the structural modes takes place at an FOF of 10Hz (see Section V). A stiffer model was constructed with the frequency of the first bending mode greater than the one obtained from the GVT (see Section IV). The new stiffer model resonates with an FOF of 15 Hz as in the experiments.

A second issue is the modelling of the static deformation at no-flow conditions due to gravity. The wing in the wind tunnel experiments is kept in the x-z plane with the pitching axis parallel to the direction of the gravity. A small twist at the tip due to gravity was observed which resulted in a static deformation of the wing in flow conditions at 0° incidence and 0° flap incidence.¹³

IV. Aeroelastic Modelling

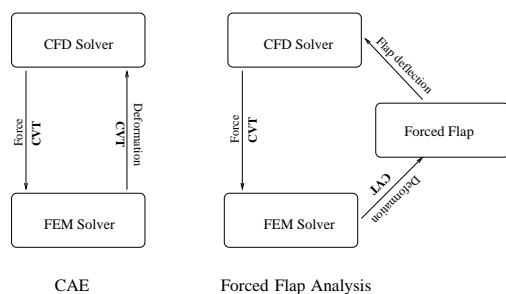


Figure 2. A typical CAE loop showing the coupling of structural and fluid solver. An intermediate step that models the forced motion of the flap is added in the current study.

a forced flap loop that includes wing flexibility. If the wing is assumed to be rigid then the FEM solver is omitted from the loop to get a purely sinusoidal oscillation of the flap. When including the wing flexibility it is important that the reduced frequency of the forced flap motion is calculated in a consistent manner with the structural reduced frequencies.

A. Forced Flap Treatment

In the current work blended flaps and flaps with free edges are used for simulations. Figure 4 shows the close-up of the two types of flap edge modelling. The flaps in the figure are deflected by an angle of 1.4° and the surface pressure contours are plotted along with the surface mesh. The gaps at the flap edges are 0.5% of the flap width and they decrease the effective surface area of the flap by 1%.

For the forced flap oscillation cases three sets of geometries are constructed. The first is the one with

0° flap deflection. The second and third have the flap deflected at $\pm 5^\circ$. Surface grids are generated on these three geometries. A flap mode shape is obtained by subtracting the coordinates of the surface grids of the geometry with flap deflected at -5° from the geometry with flap deflected at 5° . In unsteady CFD calculations the forced flap oscillation is brought about through the sinusoidal variation of the scaled flap mode shape with time. The flap mode shape contributes to the wing shape in a similar way to the structural mode shapes except that the modal coordinate is applied rather than computed from the structural model. The surface grid deformations δx_f are therefore obtained from the equation

$$\delta \mathbf{x}_s = A \sin \omega t \phi_f \quad (7)$$

where A is the amplitude of the flap oscillation, ϕ_f is the flap mode shape and ω is the frequency of the applied motion. The surface deflections due to structural modes are transformed from the structural grid and the new wing surface grid is calculated by summing the applied and structural contributions. The volume grid is recalculated by using transfinite interpolation of displacements of the surface grid deflections. The deformation of the surface grid requires a recalculation of the volume grid. This is performed with a Transfinite Interpolation (TFI) scheme that deforms the grid inside the blocks containing the deforming surface grid. This flap oscillation scheme independent of the aeroelastic module. Hence it is possible to calculate the aerodynamic quantities over the body surface with an oscillating flap assuming the body to be rigid.

B. CFD Grids

To model the effect of gaps and viscosity a total of 4 different grids have been used in this work. The viscous grid has 15 cells to resolve the boundary layer. The wall spacing is 1.8×10^{-6} chord lengths. The viscous calculations are performed only with blended flaps as there are problems with grid quality when gaps are introduced at flap edges. A C-Type grid topology is used over the wing leading edge, the wing tip and also around the fuselage. The blocks at the trailing edge are of H-Type. The C-Type blocks wrap around the rounded leading edge and the tip ensuring orthogonal cells which otherwise would be not possible with an H-H Type of blocking. The wing geometry is basically a slender delta wing on the inboard side and a collapsed triangular block is avoided at the leading edge tip by using a 3-block strategy as shown in Figure 3. Points are clustered around the trailing edge and the flap region where the shock is likely to develop and move during the buzz simulation. There are 14 cells in the chord-wise direction and 28 in span-wise direction on the flap. The size of the viscous grid is 800k cells. The grid is capable of accurately resolving the flow in the region of interest but at the same time is small enough to allow rapid turn around for the unsteady calculations. The blended Euler grids have the same topology as the viscous grid. The fine Euler grid has 1.6 million cells. There are 24 cells in the chord-wise direction and 50 span-wise. The wall spacing is 1×10^{-3} chord lengths. A coarse grid is obtained from the fine grid by removing every alternate grid point in all the three directions. The coarse Euler grid has 200k cells. The grid used for flaps with gaps is the same as the coarse Euler grid for blended flaps but with two extra blocks inside gaps between the flap edges and the wing.

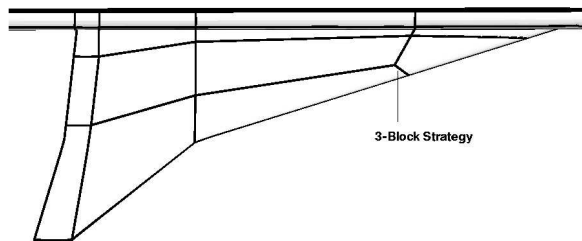


Figure 3. The 3-block strategy to avoid collapsed cells at the leading edge of wing root.

C. The FEM Model

The structural model of the wing consists of 320 triangular elements and the fuselage is made up of 2 elements which are clamped rigid. Table 1 shows the generalised mass and frequencies of the first 3 modes of the original FEM model the new stiffened model and the frequencies obtained from the GVT. Figure 5 shows the structural grid and the first three modes of the stiffened model transformed onto the surface grid. The wing deformations are primarily in the y direction and the y-coordinate contours are plotted in the figure. The first three natural modes are included in the aeroelastic calculations.

V. Results

It has been observed for the rigid BACT case that the transient dies after the first cycle with a FOF of 5 Hz.¹¹ This is not the case when flexibility is included in the computational study as the transient is determined by the time it takes for the interaction of the FOF and the vibration modes of the structure to stabilise. The duration can be anywhere between 6 to 40 cycles of the flap oscillation. Figure 6 shows the modal response of the first wing bending mode against non-dimensionalised time for the case at Mach 0.8 and incidence 0° . At the FOF of 15 Hz there is coupling of the first natural mode and the flap oscillations resulting in large deformation of the structure. The transient response is generally longer for higher FOFs.

It is observed that the structural response is sensitive to the size of the timestep at the FOF where the coupling with the structural modes takes place (which is 15 Hz for the current case). Figure 7 shows the generalised coordinate of the first mode plotted against non-dimensionalised time at Mach 0.8 and the FOFs of 15 Hz and 25 Hz respectively with two different timesteps. The timestep refinement from 0.15 to 0.06 doesn't make any difference at the FOF of 25 Hz as the two timetraces. However the amplitude of oscillation considerably increases at the FOF of 15 Hz when the timestep is decreased from 0.14 to 0.08. This sensitivity suggests that the flap has to be incremented in smaller intervals at the resonant frequency to resolve accurately the aerodynamic force over the surface.

The unsteady pressure and deformation were obtained by taking a FFT of these values at the last cycle of the flap after the transient has ended. The unsteady pressure was recorded on the upper surface at 38% and 74% wing span locations as shown in Figure 8. At 38% span the flap hinge is located at 90.5% of local chord and distinct peaks on unsteady pressure can be seen aft of this point at all FOFs. The dynamic deformation is obtained along a line originating at the wing root which is 8% semi-span including the fuselage, and 80.7% of the root chord. The line makes an angle of 113° with the x-axis.

Figure 9 shows the magnitude of unsteady dimensionless pressure and deformation in metres on a coarse grid using the Euler equations. Blended flap edges are used in the simulation. The test conditions are for Case 1 as shown in Table 2. The computed unsteady pressure and deformation have a reasonable comparison with the experiments at the resonant FOF of 15 Hz but deteriorates at FOFs above and below the resonant frequency. This might be attributed to the changes in the stiffness of the structure that were made to get resonance at 15 Hz FOF. The position and magnitude of the pressure peaks over the flap at 38% semi-span are well predicted for all FOFs. There is a considerable increase in the pressure unsteadiness at 74% semi-span which decreases from leading edge to trailing edge at the resonant frequency. This indicates the wing undergoing a twisting motion at the tip. The dynamic deformation magnitude peaks at the resonant FOF frequency of 15 Hz. The phase angle of the unsteady pressure is compared for the resonant FOF and the computed result has a lag almost 40° less than the experiments. It is found that although the timestep refinement has large effect on the amplitude of the oscillations at the resonant frequency, it does not have much effect on the phase of the unsteady pressure or dynamic deformations.

Computed results using the Euler equations for Case 2 are presented in Figure 10. A coarse grid was used for the calculations and blended flap edges are used. The unsteady pressure and deformation trends are similar to those observed in Case 1 and the computed results once again match the pressure unsteadiness well at all FOFs and both semi-span locations. As the wing is at an incidence in contrast to Case 1 the magnitude of the unsteadiness is higher. The computed dynamic deformation shows an increase of almost 20% with deformation at the tip increasing from 1 cm for Case 1 to 1.2 cm for Case 2 at the resonant frequency. As for the Case 1 the computed pressure phase angle at the two span locations is under-predicted by 40° , though the experimental trend of the phase along the chord is reproduced well in the computations.

The angle of incidence is further decreased in Case 3 to -4° and the Mach number increased to 0.9007. The flap oscillates around a mean flap angle of 5° . At these parameters a strong shock develops just aft of the flap hinge on the upper surface of the wing. Figure 11 shows the inviscid steady surface pressure coefficient contours over the wing and pressure plot at the 38% semi-span location on a fine grid. The Euler equations usually predict the shock location downstream of the real location. For the Case 3 the flap oscillates around a mean deflection angle of 5° which means that the shock for the flow modelled by the Euler equations predicts the shock oscillation over the flap, possibly unlike in the real flow. This shock oscillation over the flap is the reason for the peak in the unsteady pressure magnitude at 38% semi-span location seen in Figure 12.

The computational results for Case 1 obtained by using the original structural model are compared with the experiments in Figure 13. The wing tip undergoes the maximum dynamic deformation for all cases and FOFs. The deformation at the tip is plotted against the FOFs using the two FE models and compared

with the experiments. It can be seen that the original model resonates with the FOF of 10 Hz instead of 15 Hz and the dynamic deformation peaks at this value. It predicts the deformation accurately at FOF of 10 Hz but under-predicts the deformation for all the other FOFs. The stiffened model has a much better comparison with the experiments and follows the experimental trend. The original model is also unable to predict unsteady pressure at 74% span location

To measure the effect of the blended edges on the computed unsteady pressure and deformation an inviscid simulation is performed using flaps with free edges. Figure 14 compares the unsteady pressure and deformation for Case 2 at the FOF of 15 Hz obtained from blended flap and flap with free edges. There is little difference seen in the computed results though the blended flaps predict a slightly bigger dynamic deformation on account of it having a larger flap surface area.

The NAL-SST arrow wing has a thin section profile and for this reason the flow remains attached for most cases and for all FOFs. Viscous effects are not observed in the simulations at low incidences and the computed unsteady pressure and deformation using RANS are similar to the Euler results. Figure 15 shows the computed results from the viscous simulation for Case 1. At 38% semi-span the pressure peak over the oscillating flap is under-predicted though the location of the peak matches the experiment. The unsteady pressure at 74% semi-span and the dynamic deformation is similar to the inviscid calculations. At flow conditions where the shock does not reach the control surface it is found that the inviscid simulations are as accurate as viscous. For cases where the shock does reach the control surface, like in Case 3, viscous calculations are required to predict the shock location accurately. The shock induced separation over the oscillating control surface causes pressure redistribution and could have an effect on the structural response. Case 3 remains to be simulated using the RANS equations.

VI. Conclusion

Unsteady viscous and inviscid forced flap oscillation simulations were performed on a flexible NAL-SST arrow wing using a range of FOFs. The predicted dynamic deformation compares well with the experiments at the resonant frequency and a good comparison for unsteady pressure distribution was obtained for all frequencies. Viscous effects were found to be negligible and inviscid predictions were as accurate as viscous for the case with 0° incidence. The effect of blended flap edges on the prediction of pressure distribution and deformation of wing was found to be insignificant when compared with flaps with free edges. The FEM structural model was stiffened to allow the resonance to take place at FOF of 15 Hz. Future work could include a detailed FEM model that takes into account the positions of drilled holes.

Acknowledgements

This work was supported by BAE SYSTEMS, Engineering and Physical Sciences Research Council, Ministry of Defence and Department of Trade and Industry, and forms part of the work program of the Partnership for Unsteady Methods in Aerodynamics (PUMA) Defence and Aerospace Research Partnership (DARP). The authors would also like to thank Dr. M. Tamayama of JAXA, Japan for his insight into the problem.

References

- ¹Schuster, D. M., Liu, D. D., and Huttshell, L. J., "Computational Aeroelasticity: Success, Progress, Challenge," *Journal of Aircraft*, Vol. 40, No. 5, 2003, pp. 843–856.
- ²Bharadwaj, B. K., "Computation of Steady and Unsteady Control Surface Loads in Transonic Flow," AIAA paper 90-0935, 1990.
- ³Obayashi, S. and Guruswamy, G., "Navier-Stokes Computations for Oscillating Control Surfaces," AIAA paper 92-4431, 1992.
- ⁴Obayashi, S., Chiu, I. T., and Guruswamy, G., "Navier-Stokes Computations on Full Span Wing Body Configuration for Oscillating Control Surfaces," AIAA paper 93-3687, 1993.
- ⁵Klopper, G. H. and Obayashi, S., "Virtual Zone Navier-Stokes Computations for Oscillating Control Surfaces," AIAA paper 93-3363, 1993.
- ⁶Karlsson, A. and Winzell, B., "Unsteady Control Surface Pressure Measurements and Computations," AIAA paper 96-2417, 1996.
- ⁷Cole, H. S., Andrew, A. S., and Gupta, K., "Application of the Transpiration Method for Aeroservoelastic Prediction Using CFD," AIAA paper 98-2071, 1998.

⁸Ide, H. and Ominsky, D., "Simulation of Static and Dynamic Aeroelastic Behavior of a Flexible Wing with Multiple Control Surface," AIAA paper 90-1075, April 1990.

⁹Cole, H. S., Andrew, A. S., and Gupta, K., "CFD-Based Aeroservoelastic Predictions with Comparisons to Benchmark Experimental Data," AIAA paper 99-0766, Jan. 1999.

¹⁰Yeh, D. T., "Aeroelastic Analysis of a Hinged-Flap and Control Surface Effectiveness Using the Navier-Stokes Equations," AIAA paper 95-02263, 1995.

¹¹Schuster, D. M. and Bartels, R. E., "Benchmark Active Control Technology (BACT) Wing CFD Results," *Verification and Validation Data for Computational Unsteady Aerodynamics*, RTO Technical Report - 26, October 2000, pp. 225-238.

¹²M. Tamayama, K. Saitoh, H. M. and Nakamichi, J., "NAL SST Arrow Wing with Oscillating Flap," *Verification and Validation Data for Computational Unsteady Aerodynamics*, RTO Technical Report-26, October 2000, pp. 295-318.

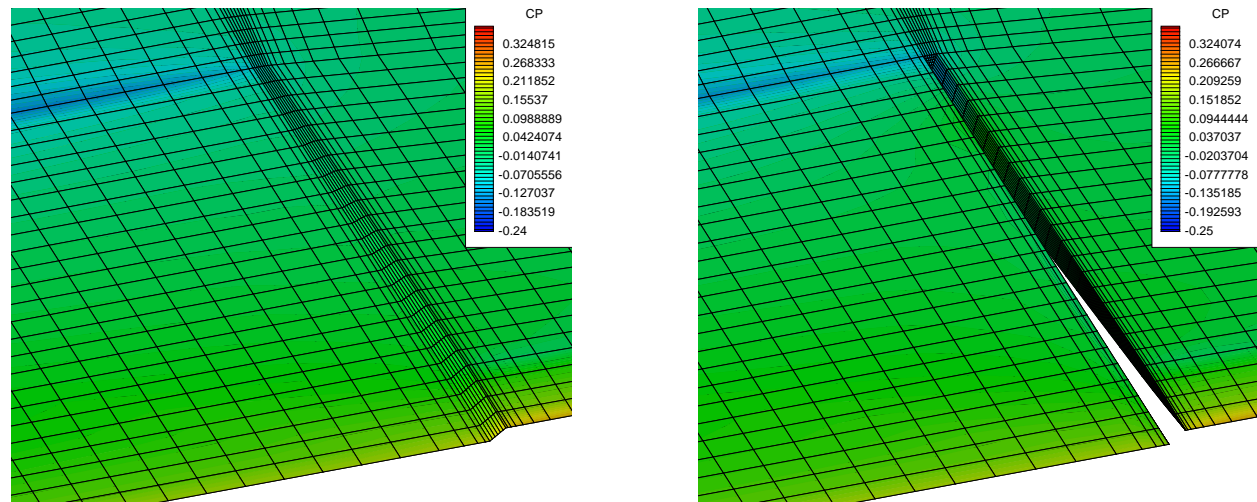
¹³Tamayama, M. and Nakamichi, J., "Unsteady Aerodynamics Measurements on an Elastic Wing Model of SST," AIAA paper 97-0836, Jan. 1997.

¹⁴Badcock, K. J., Woodgate, M. A., and Richards, B. E., "Elements of Computational Fluid Dynamics on Block Structured Grids using Implicit Solvers," *Progress in Aerospace Sciences*, Vol. 36, 2000, pp. 351-392.

¹⁵Goura, G. S. L., *Time marching analysis of flutter using Computational Fluid Dynamics*, Ph.D. thesis, University of Glasgow, 2001.

¹⁶Goura, G. S. L., Badcock, K. J., Woodgate, M. A., and Richards, B. E., "Implicit Method for the Time Marching Analysis of Flutter," *Royal Aeronautical Journal*, Vol. 105, 2001, pp. 199-214.

¹⁷Gordon, W. J. and Hall, C. A., "Construction of Curvilinear Coordinate Systems and Applications to Mesh Generation," *International Journal of Numerical Methods in Engineering*, Vol. 7, 1973, pp. 461-477.



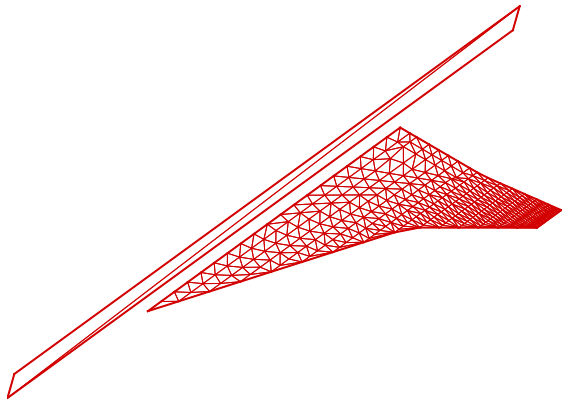
(a) Cp contours on a blended flap.

(b) Cp contours over a flap with free edges.

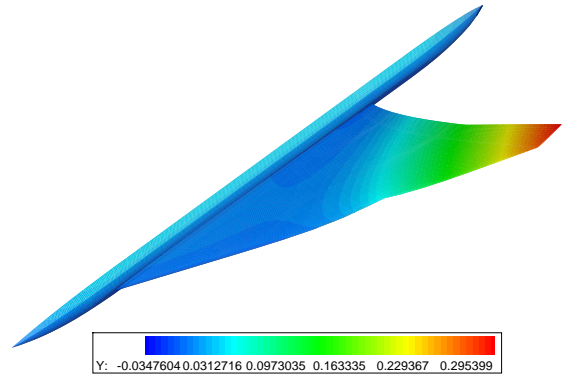
Figure 4. The two types of modelling of the flap edges.

Mode	Natural Frequencies (Hz)		
	GVT	FEM - Original	FEM - Stiffened
Mode 1 - First wing bending	9.79	11.09	12.44
-	-	41.65	-
Mode 2 - First wing twisting	40.25	44.00	51.65
Mode 3 - Second wing bending	47.91	56.26	58.32

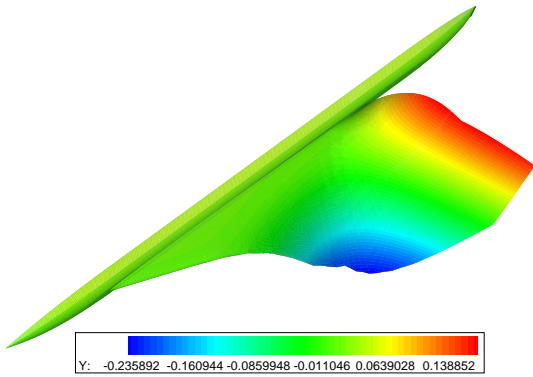
Table 1. Natural frequencies of the experimental and FEM models.



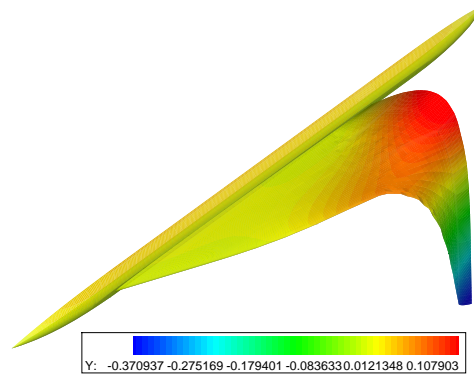
(a) Structural model



(b) Mode 1 - 12.44 Hz



(c) Mode 2 - 51.65 Hz



(d) Mode 3 - 58.32 Hz

Figure 5. The structural model and transformed mode shapes used in the simulations.

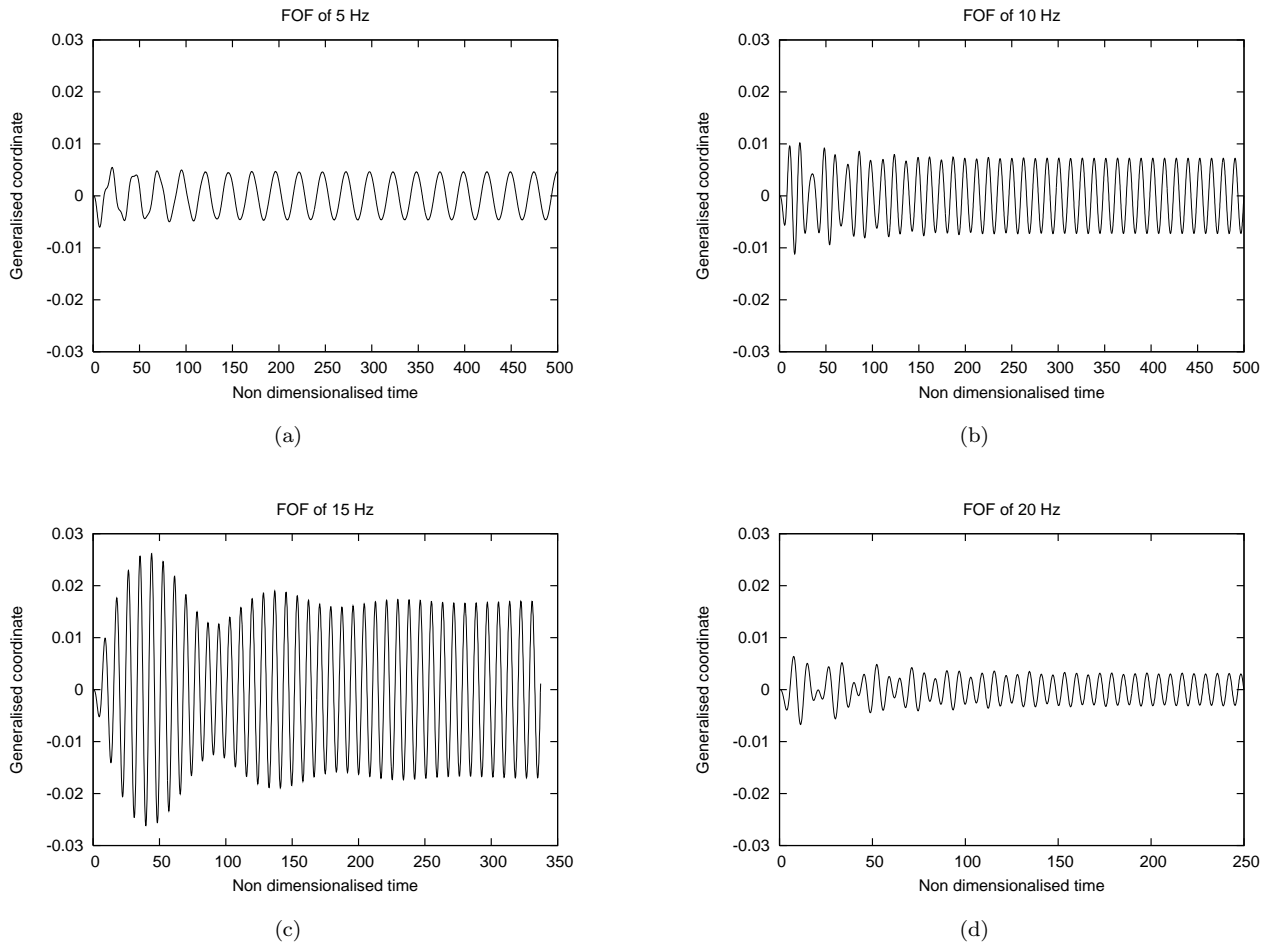


Figure 6. Number of flap cycles after which the transient dies down increases with increasing FOF.

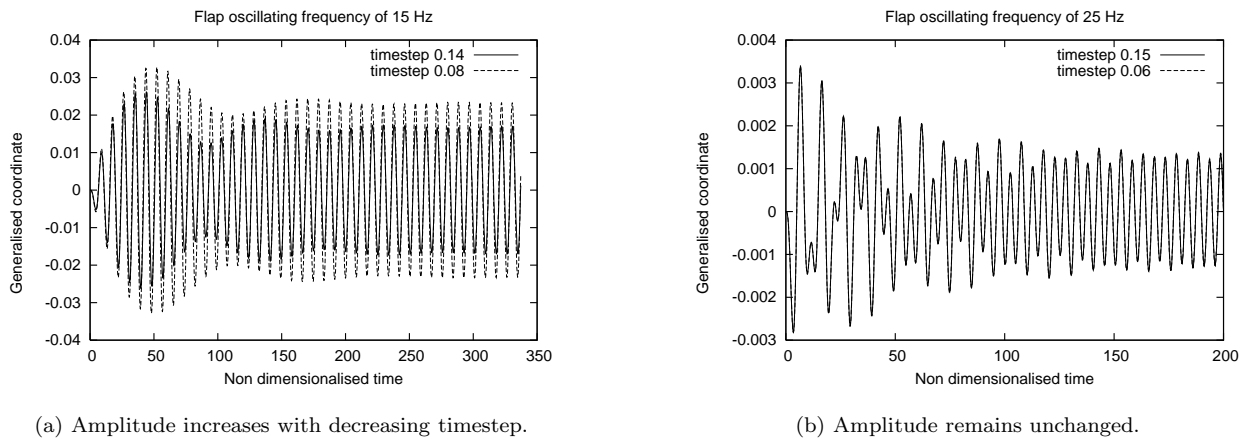
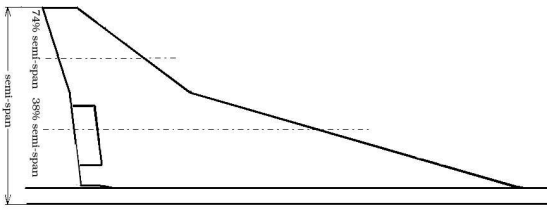
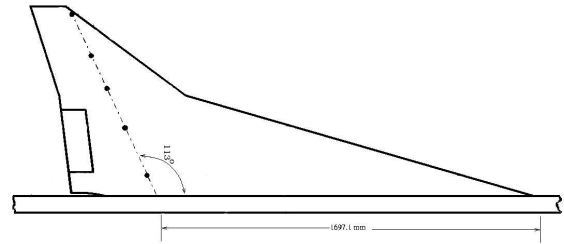


Figure 7. Sensitivity of the modal response to the timestep at the resonance FOF.

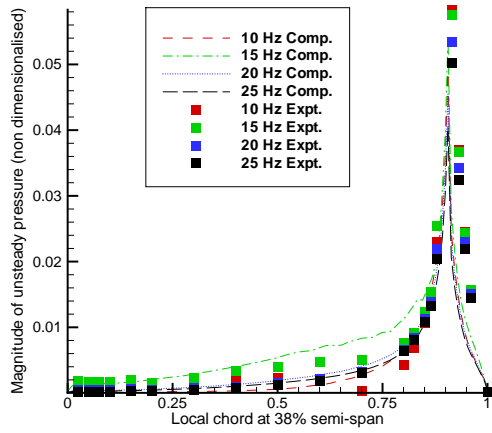


(a) Location of unsteady pressure transducers.

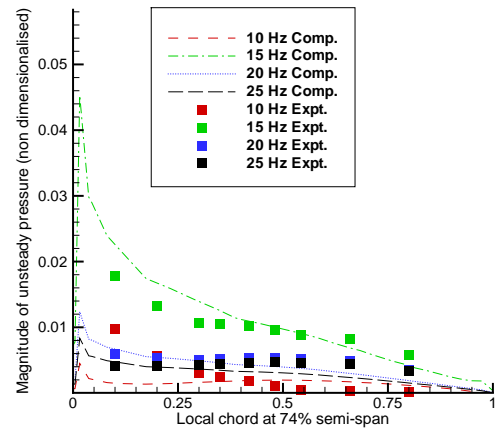


(b) Location of optical targets to measure dynamic deformation.

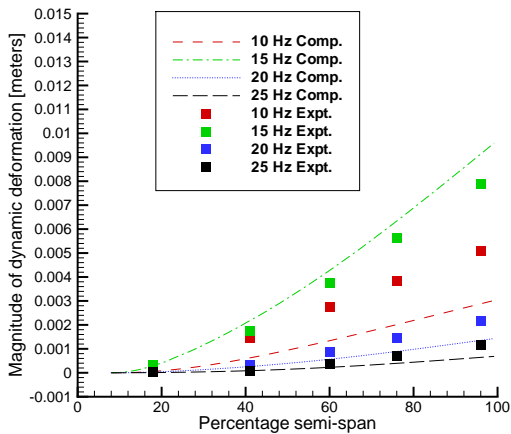
Figure 8. Location of measurement points in the experiments.



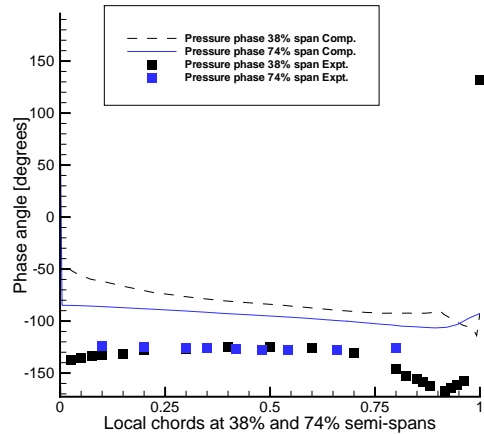
(a) Unsteady pressure at 38% semi-span location.



(b) Unsteady pressure at 74% semi-span location.

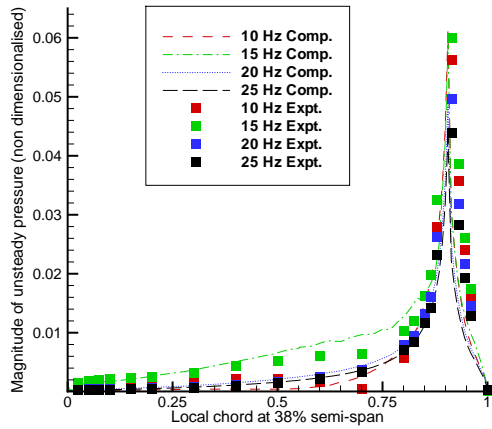


(c) Unsteady deformation along the span (see Figure 8).

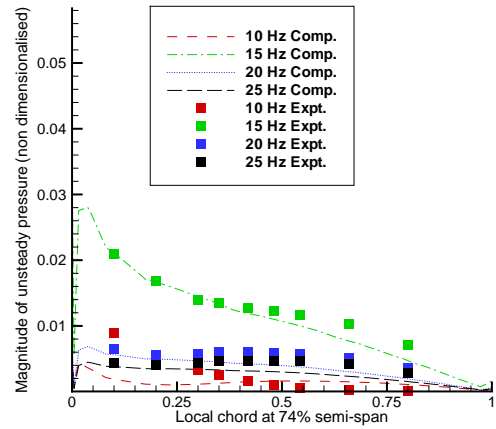


(d) Pressure phase lag at the FOF of 15 Hz

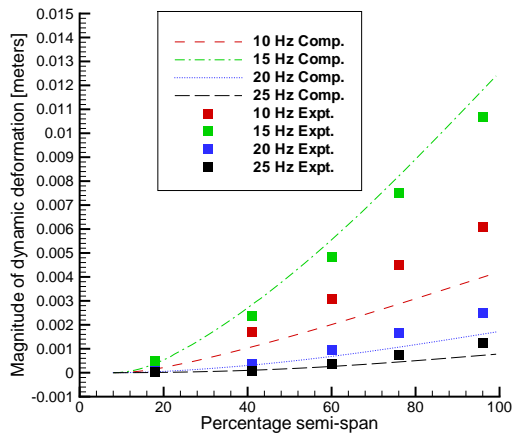
Figure 9. unsteady pressure and deformation plots for Case 1 computations on a coarse grid using Euler equations.



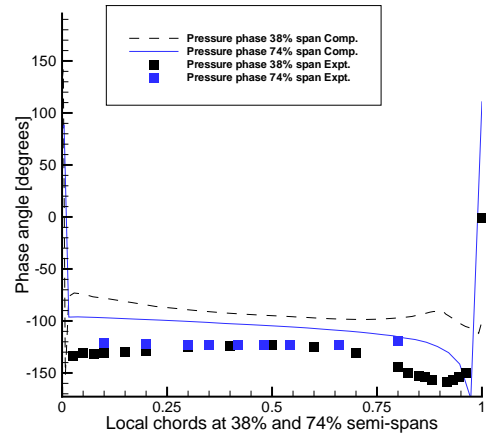
(a) Unsteady pressure at 38% semi-span location.



(b) Unsteady pressure at 74% semi-span location.



(c) Unsteady deformation along the span (see Figure 8).



(d) Pressure phase lag at the FOF of 15 Hz.

Figure 10. Unsteady pressure and deformation plots for Case 2 computations on a coarse grid using Euler equations.

	Incidence	Mean flap angle	Mach number	FOF (Hz)	Flap amplitude
Case1	0.0°	0.0°	0.8002	10	1.203°
				15	1.312°
				20	1.116°
				25	1.004°
Case2	-2.0°	0.0°	0.8009	10	1.567°
				15	1.448°
				20	1.229°
				25	1.091°
Case3	-4.0°	5.0°	0.9007	5	1.844°
				10	1.756°
				20	1.284°

Table 2. Input conditions of cases for which the results are presented.

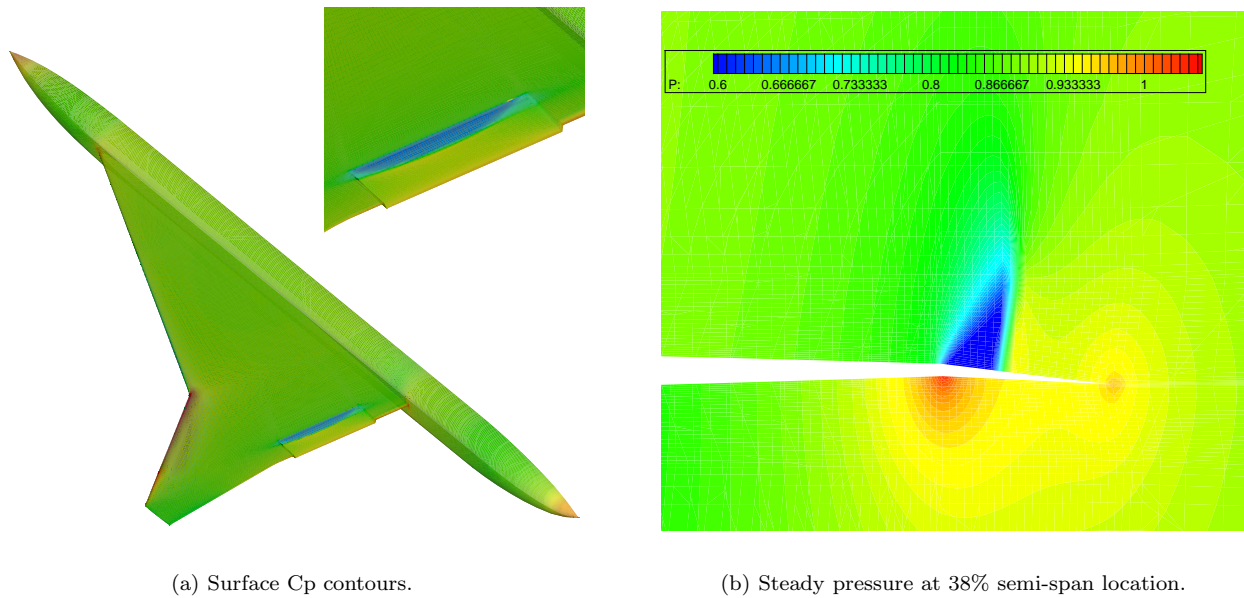
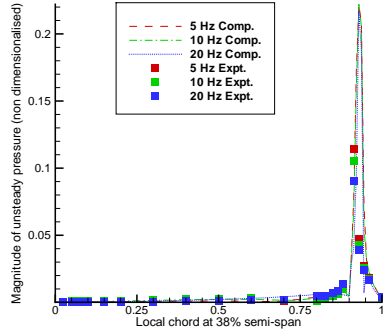
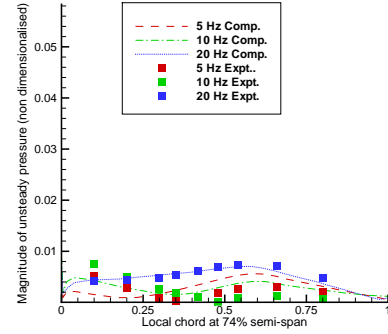


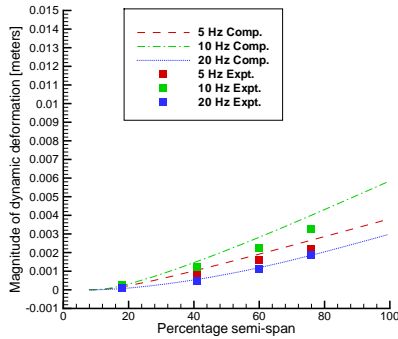
Figure 11. Steady inviscid pressure contours for Case 3. The region of low pressure at the flap leading edge has supersonic flow.



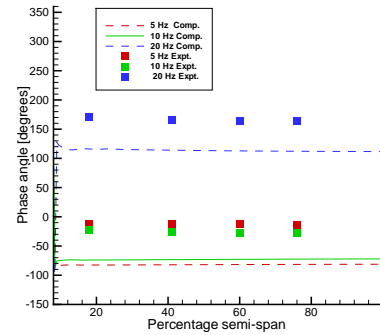
(a) Unsteady pressure at 38% semi-span location.



(b) Unsteady pressure at 74% semi-span location.

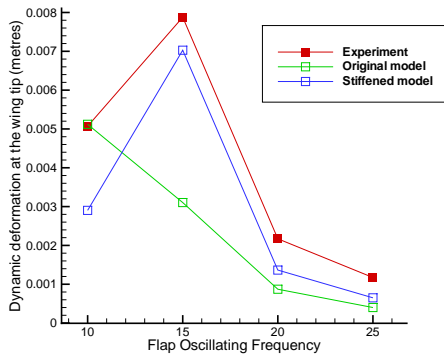


(c) Unsteady deformation along the span (see Figure 8).

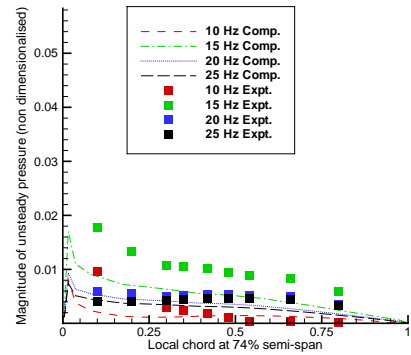


(d) Deformation phase lag at the FOFs of 5 Hz, 10 Hz and 20 Hz.

Figure 12. Unsteady pressure and deformation plots for Case 3 computations on a coarse grid using Euler equations.

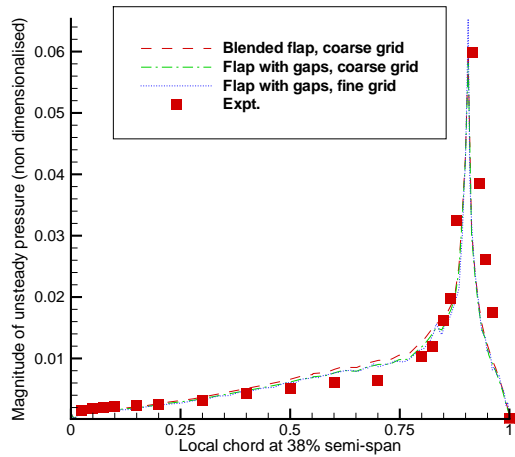


(a) Comparison of dynamic tip deformation with different FEM models.

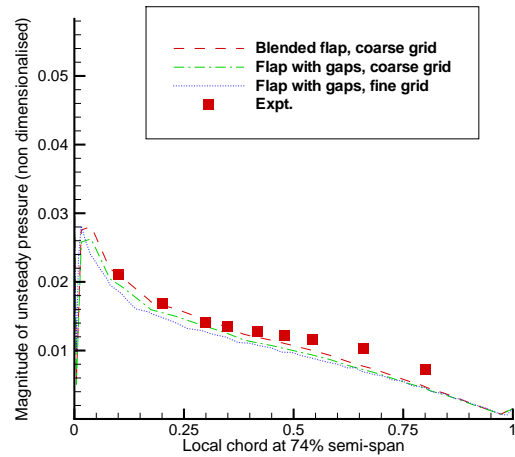


(b) Unsteady pressure at 74% semi-span location.

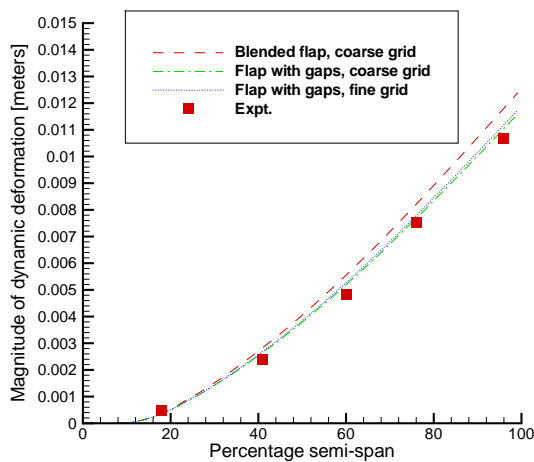
Figure 13. Comparison of unsteady pressure and deformation results between the original and the new stiffened models.



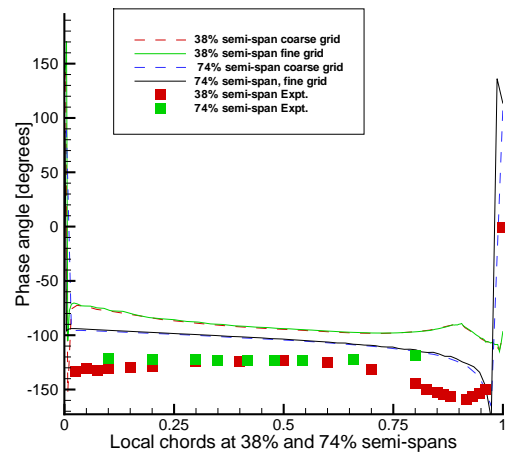
(a) Unsteady pressure at 38% semi-span location.



(b) Unsteady pressure at 74% semi-span location.

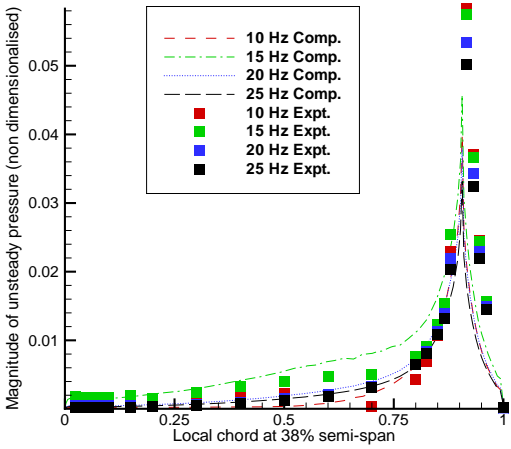


(c) Unsteady deformation along the span (see Figure 8).

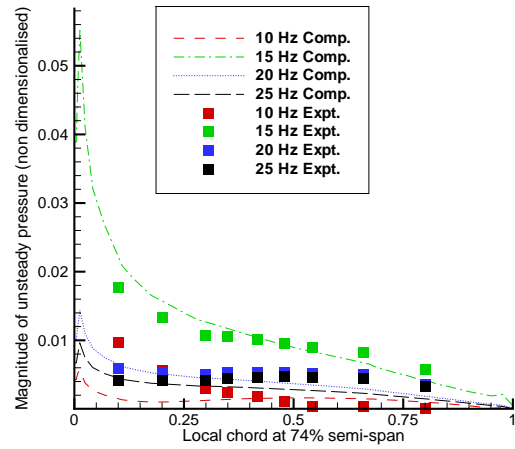


(d) Pressure phase lag of fine and coarse grids with at the FOF of 15 Hz.

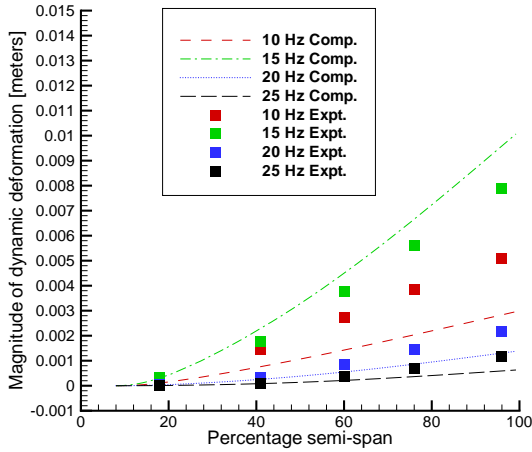
Figure 14. Unsteady pressure and deformation plots for Case 2 computations on a coarse and fine grids using flaps with gaps and at FOF of 15 Hz using the Euler equations.



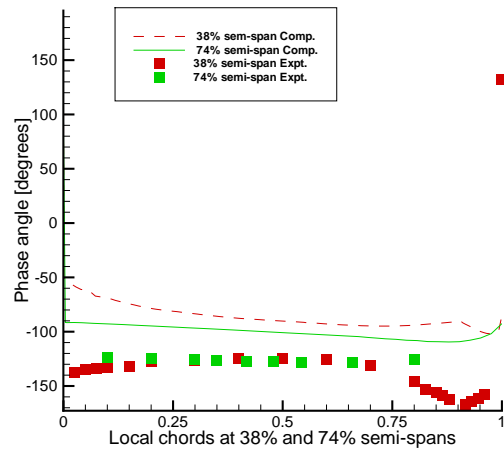
(a) Unsteady pressure at 38% semi-span location.



(b) Unsteady pressure at 74% semi-span location.



(c) Unsteady deformation along the span (see Figure 8).



(d) Pressure phase lag the FOF of 15 Hz.

Figure 15. Unsteady pressure and deformation plots for Case 1 computations using the RANS equations.